Indirect studies of electroweakly interacting particles at 100 TeV hadron colliders

Tomohiro Abe,[1,2] So Chigusa,[3] Yohei Ema,[4] and Takeo Moroi[3]

[1]*Institute for Advanced Research, Nagoya University, Furo-cho Chikusa-ku, Nagoya, Aichi 464-8602, Japan*

[2]*Kobayashi-Maskawa Institute for the Origin of Particles and the Universe, Nagoya University, Furo-cho Chikusa-ku, Nagoya, Aichi 464-8602, Japan*

[3]*Department of Physics, Faculty of Science, The University of Tokyo, Bunkyo-ku, Tokyo 113-0033, Japan*

[4]*DESY, Notkestraße 85, D-22607 Hamburg, Germany*

(Received 24 May 2019; published 16 September 2019)

There are many extensions of the standard model that predict the existence of electroweakly interacting massive particles (EWIMPs), in particular in the context of dark matter. In this paper, we provide a way to indirectly study EWIMPs through the precise study of the pair-production processes of charged leptons or that of a charged lepton and a neutrino at future 100 TeV collider experiments. It is revealed that this search method is suitable in particular for the Higgsino, providing us with a 5σ discovery reach in the supersymmetric model with a mass up to 850 GeV. We also discuss how accurately one can extract the mass, gauge charge, and spin of EWIMPs using our method.

DOI: 10.1103/PhysRevD.100.055018

I. INTRODUCTION

Electroweakly interacting massive particles (EWIMPs) are theoretically well-motivated particles that appear in many models beyond the standard model (SM). They are widely discussed in dark matter (DM) models. An attractive feature of this scenario is that the vanilla thermal freeze-out scenario predicts the correct relic abundance for the EWIMP mass range of $\mathcal{O}(1\text{–}10)$ TeV, and this mass range is within the scope of current and future experiments. Well-known examples of EWIMPs are the Higgsino and wino that arise within the supersymmetric extension of the SM. Assuming that the Higgsino (wino) is the lightest supersymmetric particle and its stability is assured by R parity, its thermal relic abundance becomes consistent with the DM abundance if the mass is 1.1 TeV [1,2] (2.9 TeV [2–5]). Another example is minimal dark matter [1,6,7], where a particle with a large $SU(2)_L$ charge is identified as DM. The stability is automatically assured since operators that cause its decay are suppressed by the cutoff scale of the theory thanks to the large $SU(2)_L$ charge, provided that one chooses the correct combination of charge and spin. A 5-plet Majorana fermion with a mass of $\mathcal{O}(10)$ TeV is the most popular in this context, but there are also other possibilities, including both scalar and fermionic particles.

EWIMPs are extensively searched for by many experiments, including direct- and indirect-detection DM and collider searches (in particular, the mono-X search and the disappearing charged track search). While EWIMPs with relatively large $SU(2)_L$ charges such as the wino and the 5-plet fermion are promising for these searches, the Higgsino is typically more challenging to probe [8]. Given this situation, another search strategy was proposed [9–16] that probes EWIMPs via electroweak precision measurements at colliders. It utilizes the pair production of charged leptons or that of a charged lepton and a neutrino, where EWIMPs affect pair-production processes through the vacuum polarizations of the electroweak gauge bosons. It is an indirect search method in the sense that it does not produce on-shell EWIMPs as final states. The current status and future prospects have been analyzed for the LHC, ILC, CLIC, and 100 TeV colliders [17–19], indicating that it provides a promising way to probe the Higgsino as well as other EWIMPs. A virtue of this method is that it is robust against the change of the lifetime and decay modes of EWIMPs and whether an EWIMP constitutes a sizable portion of the DM. Another important point is that, due to EWIMPs, the invariant mass distributions of the final-state particles show a sharp dip-like behavior at an invariant mass close to twice the EWIMP mass. This helps us to distinguish the EWIMP effects from backgrounds and systematic errors.

In this paper, we pursue this indirect search method further. In particular, we demonstrate that the indirect

search method can be applied not only to discovering EWIMPs, but also *to investigating their properties, such as charges, masses, and spins.* To be more specific, in this paper we focus on the future prospect of the indirect studies of EWIMPs at 100 TeV colliders, such as FCC-*hh* [20] and SppC [21,22]. We update our previous analysis [14] that considered only the neutral-current (NC) processes (mediated by a photon and Z boson) by including the charged-current (CC) processes (mediated by a W boson) as well, as in Refs. [15,16]. This is crucial not only to improve the sensitivity but also to break some degeneracy among different EWIMP charge assignments; the NC and CC processes depend on different combinations of the $SU(2)_L$ and $U(1)_Y$ charges, and hence the inclusion of both processes allows us to extract these charges separately.

The rest of this paper is organized as follows. In Sec. II, we discuss how EWIMPs affect the production processes of a charged lepton pair and those of a charged lepton and a neutrino. There we see that the EWIMP correction to the cross section, as a function of the lepton pair invariant mass, develops a dip-like structure when the invariant mass is around twice the EWIMP mass. This feature is essential to distinguishing the EWIMP effect from backgrounds and systematic errors, as discussed in detail in Sec. III. Although we have to rely on the transverse mass instead of the invariant mass for the CC process, a similar dip-like structure appears in the transverse mass distribution. Section III is divided into three parts. First, we explain our fitting-based statistical approach, in which we absorb various sources of systematic errors into the choice of nuisance parameters. Next, we study the result of the EWIMP detection reach, updating our previous results [14] by taking into account the CC processes. We then move to the main focus of this paper, namely, the future prospects of the mass, charge, and spin determination of the EWIMP. Finally, Sec. IV is devoted to conclusions.

II. EWIMP EFFECT ON THE LEPTON PRODUCTION PROCESSES

We investigate contributions of the EWIMPs to the Drell-Yan process through the vacuum polarization of the electroweak gauge bosons at the loop level. Throughout this paper, we assume that all of the other beyond-the-SM particles are heavy enough so that they do not affect the following discussion. After integrating out the EWIMPs, the effective Lagrangian is expressed as

$$\mathcal{L}_{\rm eff} = \mathcal{L}_{\rm SM} + C_2 g^2 W^a_{\mu\nu} f\left(-\frac{D^2}{m^2}\right) W^{a\mu\nu} + C_1 g'^2 B_{\mu\nu} f\left(-\frac{\partial^2}{m^2}\right) B^{\mu\nu}, \tag{1}$$

where $\mathcal{L}_{\rm SM}$ is the SM Lagrangian, D is a covariant derivative, m is the EWIMP mass,[1] g and g' are the $SU(2)_L$ and $U(1)_Y$ gauge coupling constants, and $W^a_{\mu\nu}$ and $B_{\mu\nu}$ are the field strengths associated with the $SU(2)_L$ and $U(1)_Y$ gauge groups, respectively. The function $f(x)$ is defined as[2]

$$f(x) = \begin{cases} \frac{1}{16\pi^2}\int_0^1 dy\, y(1-y)\ln(1-y(1-y)x-i0) & \text{(fermion)}, \\ \frac{1}{16\pi^2}\int_0^1 dy\,(1-2y)^2\ln(1-y(1-y)x-i0) & \text{(scalar)}, \end{cases} \tag{2}$$

where the first (second) line corresponds to a fermionic (scalar) EWIMP. The coefficients C_1 and C_2 for an $SU(2)_L$ n-plet EWIMP with hypercharge Y are given by

$$C_1 = \frac{\kappa}{8} n Y^2, \tag{3}$$

$$C_2 = \frac{\kappa}{8} I(n), \tag{4}$$

where $\kappa = 1, 2, 8, 16$ for a real scalar, a complex scalar, a Weyl or Majorana fermion, and a Dirac fermion, respectively. The Dynkin index $I(n)$ for the n-dimensional representation of $SU(2)_L$ is given by

$$I(n) = \frac{1}{12}(n^3 - n), \tag{5}$$

which is normalized so that $I(2) = 1/2$. The coefficients are uniquely determined by the representation of the EWIMPs. For example, $(C_1, C_2) = (1, 1)$ for the Higgsino, and $(C_1, C_2) = (0, 2)$ for the wino. We emphasize that, contrary to the usual effective field theory, our prescription can also be applied when the typical scale of the gauge boson four-momentum q is larger than the EWIMP mass scale m since we do not perform a derivative expansion of f in Eq. (1). This is important because, as we will soon see, the effects of the EWIMPs are maximized when $\sqrt{q^2} \sim m$, where the derivative expansion is not applicable.

At the leading order (LO), we are interested in $u(p)\bar{u}(p') \to \ell^-(k)\ell^+(k')$ and $d(p)\bar{d}(p') \to \ell^-(k)\ell^+(k')$ as the NC processes and $u(p)\bar{d}(p') \to \nu(k)\ell^+(k')$ and $d(p)\bar{u}(p') \to \ell^-(k)\bar{\nu}(k')$ as the CC processes. Here, u and d collectively denote up-type and down-type quarks, respectively, and p, p', k, and k' are initial- and final-state momenta. In the SM, the amplitudes for both the NC and CC processes at the LO are expressed as

[1] Here we neglect the small mass splitting among the $SU(2)_L$ multiplet.

[2] If an EWIMP interacts only through the electroweak interaction, its decay width is of $\mathcal{O}(1)\%$ or less of its mass even if it is unstable. We assume that this is the case, and neglect the small effect on the function $f(x)$ due to the small decay width.

TABLE I. Coefficients of the weak interaction defined as $\Gamma_f^{(V)} \equiv v_f^{(V)} + a_f^{(V)}\gamma_5$. Here, $e = gs_W$ and $g_Z = g/c_W$, where $s_W \equiv \sin\theta_W$ and $c_W \equiv \cos\theta_W$ with θ_W being the weak mixing angle.

Fermion f	$v_f^{(\gamma)}$	$a_f^{(\gamma)}$	$v_f^{(Z)}$	$a_f^{(Z)}$	$v_f^{(W)}$	$a_f^{(W)}$
Up-type quark	$\frac{2}{3}e$	0	$(\frac{1}{4}-\frac{2}{3}s_W^2)g_Z$	$-\frac{1}{4}g_Z$	$\frac{1}{2\sqrt{2}}g$	$-\frac{1}{2\sqrt{2}}g$
Down-type quark	$-\frac{1}{3}e$	0	$(-\frac{1}{4}+\frac{1}{3}s_W^2)g_Z$	$\frac{1}{4}g_Z$	$\frac{1}{2\sqrt{2}}g$	$-\frac{1}{2\sqrt{2}}g$
Lepton	$-e$	0	$(-\frac{1}{4}+s_W^2)g_Z$	$\frac{1}{4}g_Z$	$\frac{1}{2\sqrt{2}}g$	$-\frac{1}{2\sqrt{2}}g$

$$\mathcal{M}_{\rm SM} = \sum_V \frac{[\bar{v}(p')\gamma^\mu \Gamma_q^{(V)} u(p)][\bar{u}(k)\gamma_\mu \Gamma_\ell^{(V)} v(k')]}{s' - m_V^2}, \quad (6)$$

where $\sqrt{s'}$ is the invariant mass of the final-state leptons, which is denoted as $m_{\ell\ell}$ for the NC processes and $m_{\ell\nu}$ for the CC processes. The relevant gauge bosons are $V = \gamma, Z$ for the NC processes and $V = W^\pm$ for the CC processes, with m_V being the corresponding gauge boson mass. In addition,

$$\Gamma_f^{(V)} \equiv v_f^{(V)} + a_f^{(V)}\gamma_5, \quad (7)$$

with $v_f^{(V)}$ and $a_f^{(V)}$ given in Table I. The EWIMP contribution is given by

$$\mathcal{M}_{\rm EWIMP} = \sum_{V,V'} C_{VV'} s' f\left(\frac{s'}{m^2}\right) \times \frac{[\bar{v}(p')\gamma^\mu \Gamma_q^{(V)} u(p)][\bar{u}(k)\gamma_\mu \Gamma_\ell^{(V')} v(k')]}{(s' - m_V^2)(s' - m_{V'}^2)}, \quad (8)$$

where $C_{\gamma\gamma} = 4(C_1 g'^2 c_W^2 + C_2 g^2 s_W^2)$, $C_{\gamma Z} = C_{Z\gamma} = 4(C_2 g^2 - C_1 g'^2)s_W c_W$, $C_{ZZ} = 4(C_1 g'^2 s_W^2 + C_2 g^2 c_W^2)$, and $C_{WW} = 4C_2 g^2$. Again $V, V' = \gamma, Z$ for the NC processes and $V, V' = W^\pm$ for the CC processes.

We use $d\Pi_{\rm LIPS}$ as the Lorentz-invariant phase-space factor for the two-particle final state. Then, using Eqs. (6) and (8), we define

$$\frac{d\sigma_{\rm SM}}{d\sqrt{s'}} = \sum_{a,b} \frac{dL_{ab}}{d\sqrt{s'}} \int d\Pi_{\rm LIPS} |\mathcal{M}_{\rm SM}(q_a \bar{q}_b \to \ell\ell/\ell\nu)|^2, \quad (9)$$

$$\frac{d\sigma_{\rm EWIMP}}{d\sqrt{s'}} = \sum_{a,b} \frac{dL_{ab}}{d\sqrt{s'}} \int d\Pi_{\rm LIPS} 2\Re[\mathcal{M}_{\rm SM}\mathcal{M}^*_{\rm EWIMP}(q_a \bar{q}_b \to \ell\ell/\ell\nu)], \quad (10)$$

where we take the average and sum over the spins. Here, $dL_{ab}/d\sqrt{s'}$ is the luminosity function for a fixed $\sqrt{s'}$:

$$\frac{dL_{ab}}{d\sqrt{s'}} \equiv \frac{1}{s}\int_0^1 dx_1 dx_2 f_a(x_1) f_b(x_2) \delta\left(\frac{s'}{s} - x_1 x_2\right), \quad (11)$$

where a and b denote species of initial partons, $\sqrt{s}$ is the center-of-mass energy of the proton collision ($\sqrt{s} = 100\,\text{TeV}$ in our case), and $f_a(x)$ is the parton distribution function (PDF) of the given parton a. Equation (9) represents the SM cross section, while Eq. (10) represents the EWIMP contribution to the cross section. For the statistical treatment in the next section, we introduce a parameter μ that parametrizes the strength of the EWIMP effect, and express the cross section with μ as

$$\frac{d\tilde{\sigma}}{d\sqrt{s'}} = \frac{d\sigma_{\rm SM}}{d\sqrt{s'}} + \mu \frac{d\sigma_{\rm EWIMP}}{d\sqrt{s'}}. \quad (12)$$

Obviously, $\mu = 0$ corresponds to the pure SM, while $\mu = 1$ corresponds to the SM + EWIMP model. Hereafter, we use

$$\delta_\sigma(\sqrt{s'}) \equiv \frac{d\sigma_{\rm EWIMP}/d\sqrt{s'}}{d\sigma_{\rm SM}/d\sqrt{s'}} \quad (13)$$

to denote the correction from the EWIMP.

In Fig. 1, we plot δ_σ for the CC processes as a function of $\sqrt{s'}$. The purple, blue, and red lines correspond to the

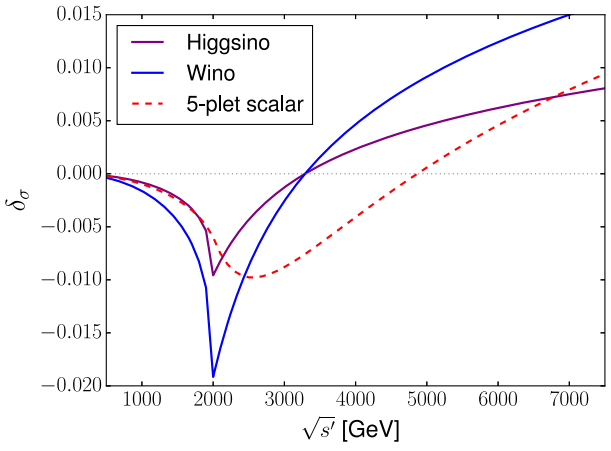

FIG. 1. δ_σ for the CC processes as a function of $\sqrt{s'} = m_{\ell\nu}$. The purple, blue, and red lines correspond to the Higgsino, wino, and 5-plet real scalar, respectively.

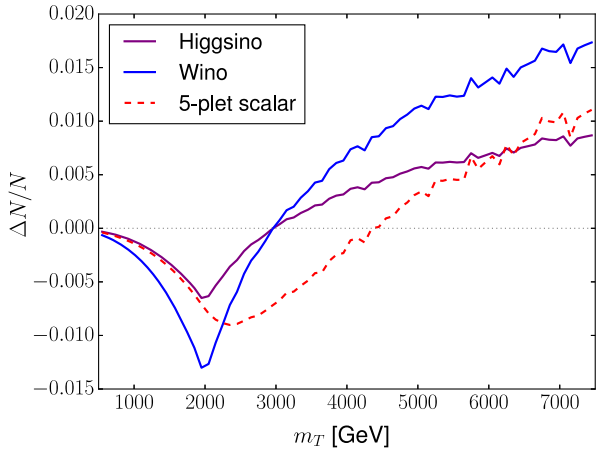

FIG. 2. The EWIMP effect on the ratio of the number of events $\Delta N/N$ as a function of m_T. The line colors are the same as in Fig. 1.

Higgsino, wino, and 5-plet scalar, respectively. There is a dip around $\sqrt{s'} = 2m$ for all of the EWIMPs which originates from the loop function f in Eq. (2). The EWIMP contributions to the NC processes show a similar dip structure that again comes from f. This dip is crucial not only for the discovery of the EWIMP signal (see Sec. III C) but also for the determination of the properties of the EWIMPs (see Sec. III D). In particular, the EWIMP mass can be extracted from the dip position, while the EWIMP charges (n and Y) can be determined from the depth of the dip.

For the NC processes, the momenta of the two final-state charged leptons are measurable and we can use the invariant mass distribution of the number of events to study the EWIMPs. For the CC processes, on the contrary, we cannot measure the momentum of the neutrino in real experiments, and hence we instead use the missing transverse momentum $p_{T,\mathrm{miss}}$. We use the transverse mass defined as

$$m_T^2 \equiv 2p_{T,\ell}p_{T,\mathrm{miss}}(1-\cos(\phi_{T,\ell,\mathrm{miss}})), \tag{14}$$

where $p_{T,\ell}$ denotes the transverse momentum of the charged lepton and $\phi_{T,\ell,\mathrm{miss}} \equiv \phi_\ell - \phi_{\mathrm{miss}}$ is the difference between the azimuthal angles of $p_{T,\ell}$ and $p_{T,\mathrm{miss}}$. The important property of m_T is that its distribution m_T peaks at $m_T = m_{\ell\nu}$. Because of this property, the characteristic shape of δ_σ remains in the m_T distribution in the CC events. To see this, in Fig. 2 we plot the EWIMP effect on the number of events as a function of m_T. Here, the vertical axis is the ratio of the EWIMP correction to the number of events ΔN to the number of events in the SM N for each bin with a bin width of 100 GeV.[3] We find that the dip structure remains in the m_T distribution, though the depth of the dip is smaller compared to the $m_{\ell\nu}$ distribution.

III. ANALYSIS

A. Event generation

Now we discuss how well we can extract information about EWIMPs from the invariant mass and transverse mass distributions for the processes of our concern at future 100 TeV pp collider experiments. We take into account the effects of the next-to-leading-order QCD corrections in the events as well as detector effects through Monte Carlo simulations.

In our analysis, we first generate the SM event sets for the NC processes $pp \to e^-e^+/\mu^-\mu^+$ and the CC processes $pp \to e^\pm\nu_e/\mu^\pm\nu_\mu$. We use MadGraph5_aMC@NLO (v2.6.3.2) [23,24] for the event generation, Pythia8 [25] for the parton shower and hadronization, and Delphes (v3.4.1) [26] with the card `FCChh.tcl` for the detector simulation. We use NNPDF2.3QED with $\alpha_s(M_Z) = 0.118$ [27] as a canonical set of PDFs. For the renormalization and factorization scales, we use the default values of MadGraph5_aMC@NLO, i.e., the central m_T^2 scale after k_T clustering of the event (which we denote by Q). The events are binned by the characteristic mass m_{char} for each process: we use the lepton invariant mass $m_{\mathrm{char}} = m_{\ell\ell}$ for the NC processes and the transverse mass $m_{\mathrm{char}} = m_T$ for the CC processes. In both cases, we generated events with characteristic masses within the range of 500 GeV $< m_{\mathrm{char}} <$ 7.5 TeV and divide them into 70 bins with an equal width of 100 GeV.

Considering the existence of the event selection by a trigger in the real experiment, we may have to impose some cut on the lepton transverse momentum p_T. As we will see, we concentrate on events with high-p_T charged lepton(s), which may trigger the event. For the NC processes, we use events with at least two high-p_T leptons. For our analysis, we use events with $m_{\ell\ell} > 500$ GeV; we assume that such events are triggered by using two energetic charged leptons so that we do not impose extra kinematical requirements. On the contrary, the CC events are characterized only by a lepton and missing transverse momentum. For such events, we require that the p_T of the charged lepton be larger than 500 GeV.[4] For the CC events, the cut reduces the number of events in particular for the bins with a low transverse mass $m_T \sim 500$ GeV, and thus affects the sensitivity of the CC processes to relatively light EWIMPs. We will come back to this point later.

[3]For illustrative purposes, we generate events corresponding to an integrated luminosity $\mathcal{L} = 1$ ab^{-1} for this figure, which is not the same luminosity that we use in the next section (see Sec. III A for details of the event generation).

[4]In the ATLAS analysis of the monolepton signal during the 2015 (2016) data-taking period [28], they used the event selection condition $p_T > 24(60)$ GeV for leptons that satisfy the *medium* identification criteria. In the CMS analysis during the 2016 data-taking period [29], they used the condition $p_T > 130(53)$ GeV for an electron (muon).

The EWIMP effect is incorporated by rescaling the SM event by δ_σ defined in Eq. (13). With the parameter μ defined in Eq. (12), the number of events corresponding to the SM + EWIMP hypothesis in the ith bin, characterized by $m_{i,\min} < m_{\rm char} < m_{i,\max}$, is

$$x_{f,i}(\mu) = \sum_{m_{i,\min}<m_{\rm char}<m_{i,\max}} [1 + \mu\delta_\sigma(\sqrt{s'})], \quad (15)$$

where the sum runs over all of the events of the final state f whose characteristic mass $m_{\rm char}$ (after taking into account the detector effects) falls into the bin. Note that the true value of $\sqrt{s'}$ should be used for each event for the computation of δ_σ: we extract it from the hard process information.[5]

B. Statistical treatment

We now explain the statistical method that we adopt in our analysis. We collectively denote our theoretical model as $\boldsymbol{x}_f(\mu) = \{x_{f,i}(\mu)\}$, where $x_{f,i}(\mu)$ is given by Eq. (15). We denote the experimental data set as $\check{\boldsymbol{x}}_f$ which in principle is completely unrelated to our theoretical model $\boldsymbol{x}_f(\mu)$. Since we do not have an actual experimental data set for 100 TeV colliders for now, we take $\check{\boldsymbol{x}}_f = \boldsymbol{x}_f(\mu = 1)$ (for some fixed values of the EWIMP mass and charges) throughout our analysis, assuming that the EWIMP does exist. In particular, this choice tests the SM-only hypothesis if we take our theoretical model as $\boldsymbol{x}_f(\mu = 0)$.

If the expectation values of $x_{f,i}(\mu)$ are precisely known, the sensitivity to EWIMPs can be studied only with statistical errors. In reality, however, the computation of $x_{f,i}(\mu)$ suffers from various uncertainties, which results in systematic errors in our theoretical model. The sources include errors in the integrated luminosity, the beam energy, choices of the renormalization and factorization scales, choices of PDFs, the pile-up effect, higher-order corrections to the cross section, and so on. In order to deal with these uncertainties, we introduce sets of free parameters $\boldsymbol{\theta}_f = \{\theta_{f,\alpha}\}$ (i.e., nuisance parameters) which absorb (smooth) uncertainties of the number of events, and modify our theoretical model as

$$\tilde{x}_{f,i}(\boldsymbol{\theta}_f, \mu) \equiv x_{f,i}(\mu) f_{{\rm sys},i}(\boldsymbol{\theta}_f), \quad (16)$$

where $f_{{\rm sys},i}(\boldsymbol{\theta}_f)$ is a function that satisfies $f_{{\rm sys},i}(\boldsymbol{0}) = 1$. We expect that, if the function $f_{{\rm sys},i}$ is properly chosen, the true distribution of the number of events in the SM is given by $\tilde{\boldsymbol{x}}_f(\boldsymbol{\theta}_f, 0) = \{\tilde{x}_{f,i}(0) f_{{\rm sys},i}(\boldsymbol{\theta}_f)\}$ for some value of $\boldsymbol{\theta}_f$. In our analysis, we adopt the five-parameter fitting function given by [30]

$$f_{{\rm sys},i}(\boldsymbol{\theta}_f) = e^{\theta_{f,1}}(1 - p_i)^{\theta_{f,2}} p_i^{(\theta_{f,3} + \theta_{f,4}\ln p_i + \theta_{f,5}\ln^2 p_i)}, \quad (17)$$

where $p_i = 2m_i/\sqrt{s}$ with m_i being the central value of the lepton invariant mass (transverse mass) of the ith bin for the NC (CC) processes. As we will see, the major effects of systematic errors can be absorbed into $\boldsymbol{\theta}_f$ with this fitting function.

In order to test the SM-only hypothesis, we define the following test statistic [31]:

$$q_0 \equiv -2 \sum_{f=\ell\bar{\ell},\ell\nu} \ln \frac{L(\check{\boldsymbol{x}}_f; \hat{\hat{\boldsymbol{\theta}}}_f, \mu = 0)}{L(\check{\boldsymbol{x}}_f; \hat{\boldsymbol{\theta}}_f, \hat{\mu})}. \quad (18)$$

Here, $\hat{\hat{\boldsymbol{\theta}}}_f$ and $\{\hat{\boldsymbol{\theta}}_f, \hat{\mu}\}$ are determined so that $\prod_f L(\check{\boldsymbol{x}}_f; \boldsymbol{\theta}_f, \mu = 0)$ and $\prod_f L(\check{\boldsymbol{x}}_f; \boldsymbol{\theta}_f, \mu)$ are maximized, respectively. The likelihood function is defined as

$$L(\check{\boldsymbol{x}}_f; \boldsymbol{\theta}_f, \mu) \equiv L_{\boldsymbol{\theta}_f}(\check{\boldsymbol{x}}_f; \mu) L'(\boldsymbol{\theta}_f; \boldsymbol{\sigma}_f), \quad (19)$$

where

$$L_{\boldsymbol{\theta}_f}(\check{\boldsymbol{x}}_f; \mu) \equiv \prod_i \exp\left[-\frac{(\check{x}_{f,i} - \tilde{x}_{f,i}(\boldsymbol{\theta}_f, \mu))^2}{2\tilde{x}_{f,i}(\boldsymbol{\theta}_f, \mu)}\right], \quad (20)$$

$$L'(\boldsymbol{\theta}_f; \boldsymbol{\sigma}_f) \equiv \prod_\alpha \exp\left[-\frac{\theta_{f,\alpha}^2}{2\sigma_{f,\alpha}^2}\right]. \quad (21)$$

The product in Eq. (20) runs over all of the bins, while the product in Eq. (21) runs over all of the free parameters we introduced. For each $\theta_{f,\alpha}$, we define the "standard deviation" $\sigma_{f,\alpha}$, which parametrizes the possible size of $\theta_{f,\alpha}$ within the SM with the systematic errors.[6] If the systematic errors are negligible compared with the statistical error, we can take $\boldsymbol{\sigma}_f \to \boldsymbol{0}$, while the analysis with $\boldsymbol{\sigma}_f \to \infty$ assumes no knowledge of systematic errors and gives a conservative result. We identify $(q_0)^{1/2} = 5$ (1.96) as the detection reach at the 5σ (95% C.L.) level, since q_0 asymptotically obeys a chi-squared distribution with one degree of freedom.

In order to determine $\boldsymbol{\sigma}_f$, we consider the following sources of systematic errors:

(1) Luminosity ($\pm 5\%$ uncertainty is assumed).
(2) Renormalization scale ($2Q$ and $Q/2$, instead of Q).
(3) Factorization scale ($2Q$ and $Q/2$, instead of Q).
(4) PDF choice [we use 101 variants of `NNPDF2.3QED` with $\alpha_s(M_Z) = 0.118$ [27] provided by LHAPDF6 [32] with IDs from 244600 to 244700].

The values of $\boldsymbol{\sigma}_f$ are determined as follows. Let $\boldsymbol{y}_f$ be the set of the number of events in the SM for the final state f with

[5]The p_T cut for the CC process does not affect this estimation since the EWIMP does not modify the angular distribution of the final lepton and neutrino for the CC process.

[6]Here we assume the Gaussian form for the nuisance parameter distribution. The dependence of the results on the choice of the distribution will be discussed later in Sec. III C.

TABLE II. Values of $\boldsymbol{\sigma}_{ee}$ for each source of systematic errors. The result is the same for the $\mu\mu$ final state.

Sources of systematic errors	$\sigma_{ee,1}$	$\sigma_{ee,2}$	$\sigma_{ee,3}$	$\sigma_{ee,4}$	$\sigma_{ee,5}$
Luminosity: $\pm 5\%$ ($\boldsymbol{\sigma}_{ee}^{\mathrm{lumi}}$)	0.05	0	0	0	0
Renormalization scale: $2Q, Q/2$ ($\boldsymbol{\sigma}_{ee}^{\mathrm{ren}}$)	0.4	0.6	0.3	0.05	0.004
Factorization scale: $2Q, Q/2$ ($\boldsymbol{\sigma}_{ee}^{\mathrm{fac}}$)	0.3	0.5	0.2	0.06	0.004
PDF choice ($\boldsymbol{\sigma}_{ee}^{\mathrm{PDF}}$)	0.4	0.7	0.3	0.06	0.004

the canonical choices of the parameters, and $\boldsymbol{y}'_f$ be that with one of the sources of the systematic errors being varied. We minimize the chi-squared function defined as

$$\chi^2_f \equiv \sum_i \frac{(y'_{f,i} - \tilde{y}_{f,i}(\boldsymbol{\theta}_f))^2}{\tilde{y}_{f,i}(\boldsymbol{\theta}_f)}, \tag{22}$$

where

$$\tilde{y}_{f,i}(\boldsymbol{\theta}_f) \equiv y_{f,i} f_{\mathrm{sys},i}(\boldsymbol{\theta}_f) \tag{23}$$

for each final state f, and determine the best-fit values of $\boldsymbol{\theta}_f$ for each set of $\boldsymbol{y}'_f$. We repeat this process for different sets of $\boldsymbol{y}'_f$, and $\boldsymbol{\sigma}_f$ are determined from the distributions of the best-fit values of $\boldsymbol{\theta}_f$. For example, let us denote the best-fit values for the fit associated with the luminosity errors $\pm 5\%$ as $\boldsymbol{\theta}_f^{\pm}$. We estimate the $\boldsymbol{\sigma}_f$ associated with these errors, denoted here as $\boldsymbol{\sigma}_f^{\mathrm{lumi}}$, as

$$\sigma_{f,\alpha}^{\mathrm{lumi}} = \sqrt{\frac{(\theta_{f,\alpha}^{+})^2 + (\theta_{f,\alpha}^{-})^2}{N}}, \tag{24}$$

where N denotes the number of fitting procedures we have performed ($N = 2$ for this case). We estimate the $\boldsymbol{\sigma}_f$ associated with the other sources of errors, denoted as $\boldsymbol{\sigma}_f^{\mathrm{ren}}$, $\boldsymbol{\sigma}_f^{\mathrm{fac}}$, and $\boldsymbol{\sigma}_f^{\mathrm{PDF}}$, in a similar manner. Finally, the total values of the $\boldsymbol{\sigma}_f$ are obtained by combining all of the sources together as[7]

$$\sigma_{f,\alpha} = \sqrt{(\sigma_{f,\alpha}^{\mathrm{lumi}})^2 + (\sigma_{f,\alpha}^{\mathrm{ren}})^2 + (\sigma_{f,\alpha}^{\mathrm{fac}})^2 + (\sigma_{f,\alpha}^{\mathrm{PDF}})^2}. \tag{25}$$

In Tables II and III, we show the values of $\boldsymbol{\sigma}_{ee}$ and $\boldsymbol{\sigma}_{e\nu_e}$ associated with each source of systematic errors, respectively. These values can be interpreted as the possible size of the fit parameters within the SM, which is caused by the systematic uncertainties. As explained in Eq. (25), we combine these values in each column to obtain $\boldsymbol{\sigma}_f$. In Table IV, we summarize the result of the combination for all of the final states. The values of $\boldsymbol{\sigma}_f$ are independent of the final-state lepton flavors since the energy scale of our concern is much higher than the lepton masses. However, we use different sets of fit parameters—$\boldsymbol{\theta}_{ee}$ and $\boldsymbol{\theta}_{\mu\mu}$ for the NC processes and $\boldsymbol{\theta}_{e\nu_e}$ and $\boldsymbol{\theta}_{\mu\nu_\mu}$ for the CC processes—because of the different detector responses to electrons and muons.

[7]There may be some correlations between the distributions of the nuisance parameters $\boldsymbol{\theta}_f$. In this paper, we assume that each one obeys an independent Gaussian distribution for simplicity.

TABLE III. Best-fit values of fit parameters for several sources of systematic errors for the $e\nu_e$ final state. The result is the same for the $\mu\nu_\mu$ final state.

Sources of systematic errors	$\sigma_{e\nu_e,1}$	$\sigma_{e\nu_e,2}$	$\sigma_{e\nu_e,3}$	$\sigma_{e\nu_e,4}$	$\sigma_{e\nu_e,5}$
Luminosity: $\pm 5\%$ ($\boldsymbol{\sigma}_{e\nu_e}^{\mathrm{lumi}}$)	0.05	0	0	0	0
Renormalization scale: $2Q, Q/2$ ($\boldsymbol{\sigma}_{e\nu_e}^{\mathrm{ren}}$)	0.3	0.4	0.2	0.04	0.003
Factorization scale: $2Q, Q/2$ ($\boldsymbol{\sigma}_{e\nu_e}^{\mathrm{fac}}$)	1.0	1.6	0.6	0.1	0.01
PDF choice ($\boldsymbol{\sigma}_{e\nu_e}^{\mathrm{PDF}}$)	0.6	0.9	0.4	0.08	0.006

TABLE IV. Summary of the standard deviations $\boldsymbol{\sigma}_f$ for each final state.

Final state f	$\sigma_{f,1}$	$\sigma_{f,2}$	$\sigma_{f,3}$	$\sigma_{f,4}$	$\sigma_{f,5}$
ee	0.7	1.0	0.4	0.09	0.008
$\mu\mu$	0.7	1.0	0.4	0.09	0.008
$e\nu_e$	1.2	1.9	0.7	0.2	0.01
$\mu\nu_\mu$	1.2	1.9	0.7	0.2	0.01

In the tables, we neglect the systematic errors from the detector effect. The main errors are expected to come from the lepton identification, in which some of the leptons in any process are overlooked or identified incorrectly, resulting in the misreconstruction of the event topology. Since we perform the fitting procedure using Eq. (18), it is expected that the small and smooth modification of the number of events as a function of the lepton invariant mass may be absorbed into the choice of nuisance parameters, if the corresponding values of $\boldsymbol{\sigma}_f$ are properly taken into account in addition to the values in Table II. What is dangerous is the possible jerky modification that mimics the EWIMP signal, which may be induced by the detector setup, the complicated detector response to leptons, and so on. In this paper, we just assume that these systematic errors from the detector effect will be well controlled once the real experiment starts, and focus on the theoretical uncertainties listed in the tables.

C. Detection reach

Now we show the detection reach of EWIMPs at future 100 TeV colliders. In Fig. 3, we plot the value of $\sqrt{q_0}$ as a function of the EWIMP mass, with the integrated

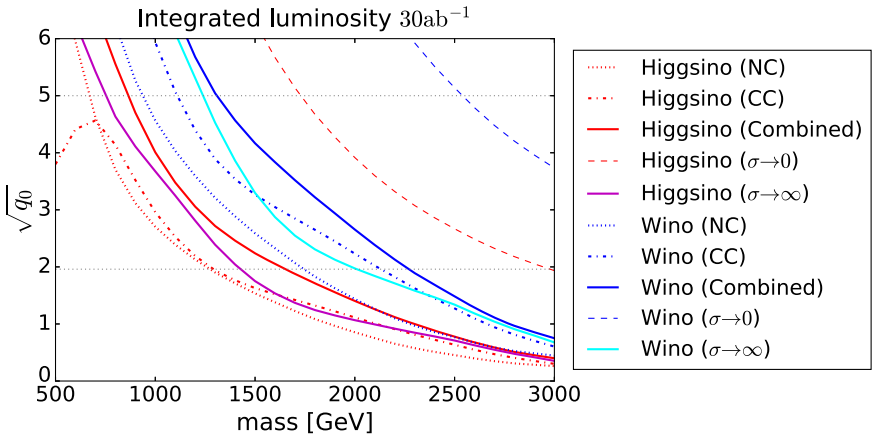

FIG. 3. $\sqrt{q_0}$ as a function of the EWIMP mass. Red and blue lines correspond to the Higgsino and wino, respectively, while line styles represent the result from the NC processes, the CC processes, the combined analysis, and the combined analysis with the optimistic $\boldsymbol{\sigma}_f \to \mathbf{0}$ limit. The purple and cyan lines correspond to the results from the conservative analysis with $\boldsymbol{\sigma}_f \to \infty$ for the Higgsino and wino, respectively.

luminosity $\mathcal{L} = 30$ ab^{-1}. As representative scenarios, we show the cases for the Higgsino (red lines) and wino (blue lines). The dotted and dash-dotted lines are the results obtained only from the NC processes and CC processes, respectively. We find that the CC processes are more sensitive to the effect of the EWIMPs than the NC processes because of the larger cross section. This result is consistent with Refs. [15,16]. The sensitivity of the CC processes is weakened for $m \lesssim 700$ GeV because of the lepton p_T cut we have applied.[8] The combined results of the NC and CC processes are shown by the solid lines. By combining the two types of processes, the 5σ discovery reaches (95% C.L. bounds) for he Higgsino and wino are 850 GeV (1.7 TeV) and 1.3 TeV (2.3 TeV), respectively. We find that the combination of the NC and CC processes improves the sensitivity of the EWIMP mass. Furthermore, if we understand all of the systematic uncertainties quite well and effectively take the $\boldsymbol{\sigma}_f \to \mathbf{0}$ limit in the combined result, the detection reach will be pushed up significantly as shown by the dashed lines: a 1.1 TeV Higgsino signal at well above the 5σ level, and a 4σ hint of the 2.9 TeV wino. These lines should be compared with the combined results and also with those obtained from the conservative analysis with $\boldsymbol{\sigma}_f \to \infty$, assuming no knowledge about the sources of systematic errors. The plot shows us that it is essential to reduce the systematic uncertainties for the detection of EWIMPs through the NC and CC processes.

So far, we have assumed that the distribution of the nuisance parameters has a Gaussian form and that the fitting function (17) is sufficient to treat the systematic errors. In order to discuss the dependence of the results on these assumptions, we have repeated the same analysis using another distribution or fitting function. In the former case, we have adopted the top-hat distribution: the likelihood function for the nuisance parameters L' is given by

$$L'(\boldsymbol{\theta}_f;\boldsymbol{\sigma}_f) \equiv \prod_\alpha \Theta(\sqrt{3}\sigma_{f,\alpha} - |\theta_{f,\alpha}|), \tag{26}$$

where Θ is the Heaviside step function. This corresponds to the top-hat distribution of $\theta_{f,\alpha}$ with a variance $\sigma^2_{f,\alpha}$ for each α. As an example of another fitting function, we have adopted a simple one-parameter extension of Eq. (17),

$$f_{\mathrm{sys},i}(\boldsymbol{\theta}_f) = e^{\theta_{f,1}}(1-p_i)^{\theta_{f,2}} p_i^{(\theta_{f,3}+\theta_{f,4}\ln p_i+\theta_{f,5}\ln^2 p_i+\theta_{f,6}\ln^3 p_i)}, \tag{27}$$

which consists of six parameters. The variances of the nuisance parameters are estimated in the same way as in Sec. II B, but now with six parameters.

In Fig. 4 we show the corresponding results. The convention for the line colors is the same as in Fig. 3, while the lines denote different procedures: the dashed and dotted lines correspond to the results with the top-hat distribution and the six-parameter fitting function, respectively, while the solid lines are the same as in Fig. 3. From the figure, we can see that the choice of the distribution may slightly affect the result, while the addition of a nuisance parameter [as in Eq. (27)] has almost no effect. The size of the effect of the choice of the distribution for the current estimation of errors $\boldsymbol{\sigma}_f$ is about 100 GeV (200 GeV) for the 5σ (95% C.L.) bounds. We expect that such uncertainties from the choice of the distribution and fitting function will be reduced once the data from the real experiment (and hence better understanding of the systematic errors) will become available.

[8]We note here that the sensitivity of the CC processes depends on the lepton p_T cut. For example, adopting the tighter cut (lepton $p_T > 1$ TeV), the CC processes have almost no sensitivity to EWIMPs with $m < 1$ TeV. Thus, in particular for the Higgsino search, it is important to have a lepton p_T cut as low as ~500 GeV.

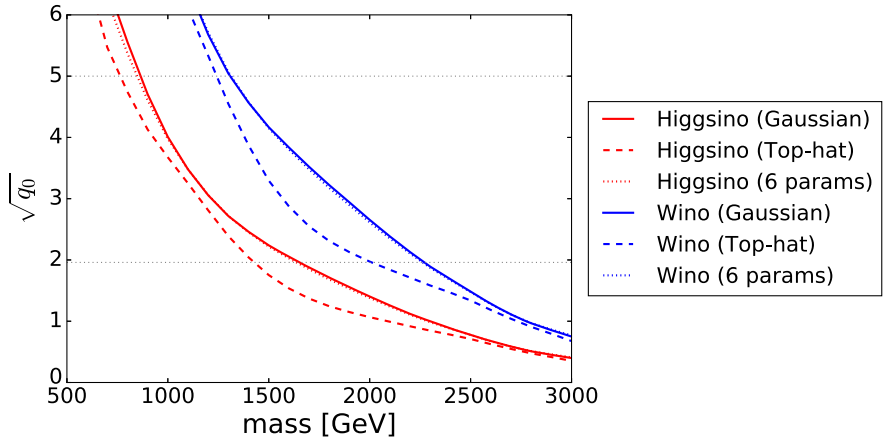

FIG. 4. $\sqrt{q_0}$ as a function of the EWIMP mass using both the NC and CC processes. The convention for the line colors is the same as in Fig. 3. The lines denote the same result as in Fig. 3 (solid), that with the top-hat distribution (dashed), and that with the six parameters fitting function (dotted).

D. Determination of EWIMP properties

In this subsection, we show that it is possible to determine the properties of the EWIMPs from the NC and CC processes, thanks to the fact that we can study the $m_{\ell\ell}$ and m_T distributions in great detail for these processes. Some information about the masses, charges, and spins of the EWIMPs can be extracted because the corrections to these distributions from the EWIMPs are completely determined by these EWIMP properties. First, we can extract the EWIMP mass from the position of the dip-like structure in the correction since it corresponds to roughly twice the EWIMP mass, as we have shown in Sec. II. Second, the overall size of the correction gives us information about the $SU(2)_L$ and $U(1)_Y$ charges. The CC processes depend on only the $SU(2)_L$ charge, while the NC processes depend on both the $SU(2)_L$ and $U(1)_Y$ charges. Consequently, we can obtain information about the gauge charges of the EWIMPs from the NC and CC processes.

We now demonstrate the mass and charge determination of fermionic EWIMPs. This is equivalent to the determination of the parameter set (m, C_1, C_2). We generate the data assuming the SM + EWIMP model ($\mu = 1$) with some specific values of m, n, Y, and κ, with which we obtain (m, C_1, C_2). We fix $\mu = 1$ for our theoretical model as well, and hence the theoretical predictions of the number of events also depend on these three parameters, $\boldsymbol{x}_f = \boldsymbol{x}_f(m, C_1, C_2)$. We define the likelihood function $L(\check{\boldsymbol{x}}_f; \boldsymbol{\theta}_f, m, C_1, C_2)$ in the same form as Eqs. (16) and (19) with the theoretical prediction $\boldsymbol{x}_f$ now understood as a function of (m, C_1, C_2), not of μ.[9]

The test statistic is defined as

$$q(m, C_1, C_2) \equiv -2\sum_f \ln \frac{L(\check{\boldsymbol{x}}_f; \hat{\hat{\boldsymbol{\theta}}}_f, m, C_1, C_2)}{L(\check{\boldsymbol{x}}_f; \hat{\boldsymbol{\theta}}_f, \hat{m}, \hat{C}_1, \hat{C}_2)}, \tag{28}$$

where the parameters $(\{\hat{\boldsymbol{\theta}}_f\}, \hat{m}, \hat{C}_1, \hat{C}_2)$ maximize $\prod_f L(\check{\boldsymbol{x}}_f; \boldsymbol{\theta}_f, m, C_1, C_2)$, while $\hat{\hat{\boldsymbol{\theta}}}_f$ maximize $L(\check{\boldsymbol{x}}_f; \boldsymbol{\theta}_f, m, C_1, C_2)$ for fixed values of (m, C_1, C_2). It follows a chi-squared distribution with three degrees of freedom in the limit of a large number of events [33]. The test statistic defined in this way examines the compatibility of a given EWIMP model [i.e., a parameter set (m, C_1, C_2)] with the observed signal.

Once a deviation from the SM prediction is observed in a real experiment, we may determine (m, C_1, C_2) using the above test statistic q. In the following, we show the

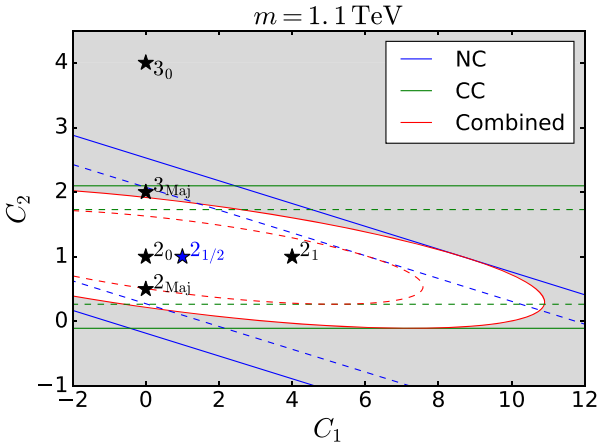

FIG. 5. Contour of $\sqrt{q}$ in the C_1 vs C_2 plane with $m = 1.1$ TeV, where we assume a 1.1 TeV Higgsino signal. The dotted and solid lines denote the 1σ and 2σ contours, respectively, and the gray region corresponds to the parameter space that is in tension with the observation beyond the 2σ level. The blue, green, and red lines correspond to the results from the NC processes, the CC processes, and the combined analysis, respectively. Each star labeled with "n_Y" represents a point corresponding to a $SU(2)_L$ n-plet Dirac fermion with hypercharge Y, while those with "$n_{\rm Maj}$" correspond to an $SU(2)_L$ n-plet Majorana fermion.

[9]As shown in Eqs. (3) and (4), C_1 and C_2 are positive quantities (and C_2 is discrete). In the figures, however, we extend the C_1 and C_2 axes down to negative regions just for presentation purposes.

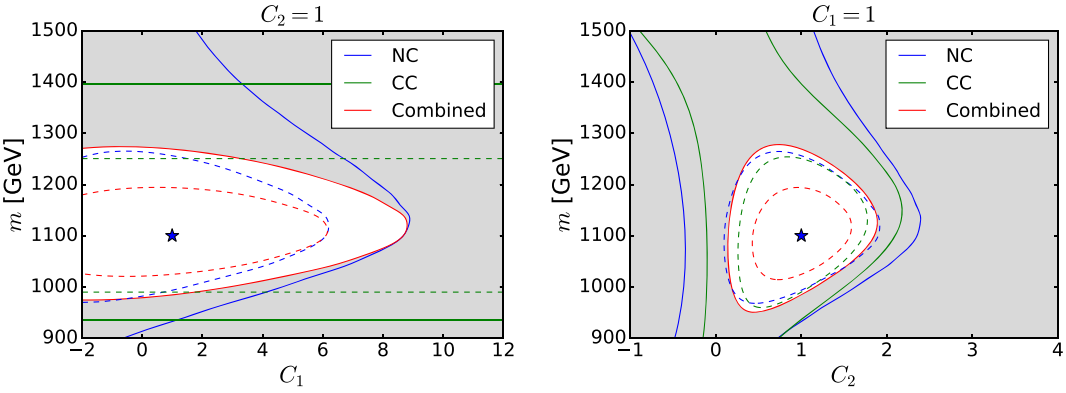

FIG. 6. Left: Contour of $\sqrt{q}$ in the C_1 vs m plane with $C_2 = 1$, where we assume a 1.1 TeV Higgsino signal. The colors and styles of lines and the meaning of the gray region are the same as in Fig. 5. The star corresponds to the true Higgsino property $(C_1, m) = (1, 1.1\ \text{TeV})$. Right: Contour of $\sqrt{q}$ in the C_2 vs m plane for $C_1 = 1$, where we assume a 1.1 TeV Higgsino signal. The star corresponds to the true Higgsino property $(C_2, m) = (1, 1.1\ \text{TeV})$.

expected accuracy of the determination of (m, C_1, C_2) for the case where there is a 1.1 TeV Higgsino.[10]

In Fig. 5, we show the contours of the 1σ (dotted) and 2σ (solid) constraints, which correspond to the values $\sqrt{q} = 1.9$ and $\sqrt{q} = 2.8$, respectively, in the C_1 vs C_2 plane for $m = 1.1$ TeV. The blue, green, and red lines denote the results obtained from the NC processes, the CC processes, and the combined analysis, respectively. The models in the gray region are in more than 2σ tension with the observation. We also show points (marked with stars) that correspond to the single $SU(2)_L$ multiplet contributions: those with "n_Y" represent an $SU(2)_L$ n-plet Dirac fermion with hypercharge Y, while those with "n_{Maj}" represent an $SU(2)_L$ n-plet Majorana fermion. Both the NC and CC constraints are represented as straight bands in the C_1 vs C_2 plane since each process depends on a specific linear combination of C_1 and C_2. In particular, the CC constraint is independent of C_1, or Y. In this sense, the NC and CC processes are complementary to each other, and thus we can separately constrain C_1 and C_2 only after combining these two results. For instance, we can exclude a single fermionic $SU(2)_L$ multiplet with $n \neq 2$ beyond the 2σ level, although each process by itself cannot exclude the possibility of 3_{Maj}. We can also constrain the hypercharge, yet it is not uniquely determined. In addition to the Higgsino, the EWIMP as an $SU(2)_L$ doublet Dirac fermion with $|Y|^2 \lesssim 2$ or an $SU(2)_L$ doublet Majorana fermion with $|Y|^2 \lesssim 5$ is still allowed.

In Fig. 6, we show the contour plots of $\sqrt{q}$ in the C_1 vs m plane with $C_2 = 1$ (left) and those in the C_2 vs m plane with $C_1 = 1$ (right). The star in each panel shows the true values of the parameters $(C_1, m) = (1, 1.1\ \text{TeV})$ (left) and $(C_2, m) = (1, 1.1\ \text{TeV})$ (right). Again, by combining the NC and CC results, we can significantly improve the determination of EWIMP properties, making 1σ and 2σ contours in the planes of our concern. In particular, as the red lines show, the combined analysis allows us to determine the observed EWIMP mass at the level of $\mathcal{O}(10)\%$.

Finally, we comment on the possibility of discriminating between fermionic and scalar EWIMPs, whose difference comes from the loop function $f(x)$ [see Eq. (2)]. Here we repeat the same analysis explained above, assuming a 1.1 TeV Higgsino signal for example, but use the scalar loop function to evaluate the theoretical predictions $\boldsymbol{x}_f(m, C_1, C_2)$. In Figs. 7 and 8, we show the results in the C_1 vs C_2 plane and the C_1 (or C_2) vs m plane, respectively, where one of the three parameters is fixed to its best-fit value. It is seen that, in the case of a 1.1 TeV Higgsino signal, it is hard to distinguish between the

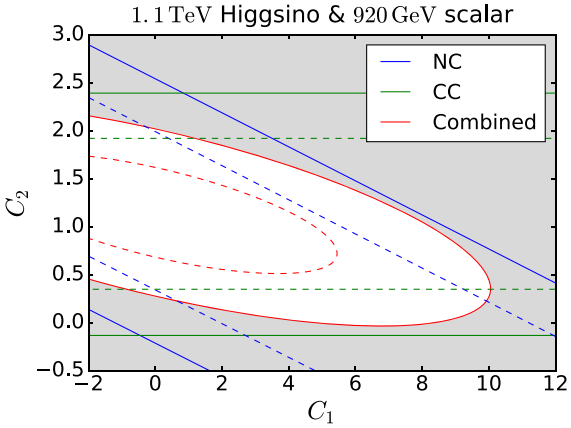

FIG. 7. Contour of $\sqrt{q}$ in the C_1 vs C_2 plane for a 1.1 TeV Higgsino signal, tested with the 920 GeV scalar EWIMP assumption. The colors and styles of lines and the meaning of the gray region are the same as in Fig. 5.

[10]The expected significance is 3.5σ for a 1.1 TeV Higgsino in our estimation. Even though it is slightly below the 5σ discovery level, we take a 1.1 TeV Higgsino as an example because it is a candidate for thermal relic DM.

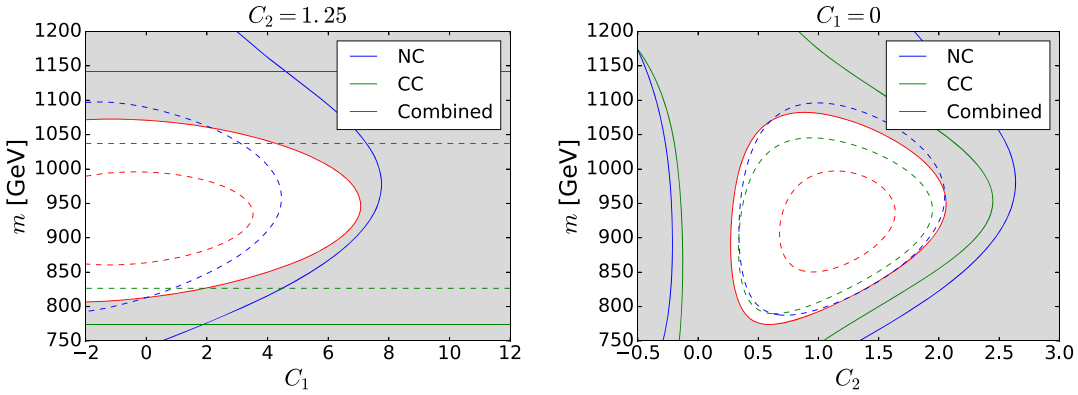

FIG. 8. Left: Contour of $\sqrt{q}$ in the C_1 vs m plane with $C_2 = 1.25$ for a 1.1 TeV Higgsino signal, tested with the scalar EWIMP assumption. The colors and styles of lines and the meaning of the gray region are the same as in Fig. 5. Right: Contour of $\sqrt{q}$ in the C_2 vs m plane with $C_1 = 0$ for a 1.1 TeV Higgsino signal, tested with the scalar EWIMP assumption.

bosonic and fermionic EWIMPs with our method alone. However, if one of the EWIMP properties (in particular, its mass) is determined from another approach, our method may allow us to determine its spin correctly.

We also stress here that, with some favorable assumptions about the observed signal, we may obtain some hint about its spin. For example, if we assume that the observed signal composes a fraction of the dark matter in our Universe, the choice of the EWIMP charges is significantly constrained. Note from Fig. 7 that the only choices of EWIMP charges that allow the EWIMP multiplet to contain an electrically neutral component are $(n, |Y|) = (3, 0), (3, 1), (4, 1/2), (4, 3/2)$, and $(5, 0)_{\text{real}}$. The last column of Table V shows choices for the EWIMP masses that make their thermal relic abundances comparable with the dark matter abundance in the current Universe. All of these values are somewhat larger than the central value of the mass of the observed signal, which means that the scalar interpretation of the signal cannot explain the entire dark matter relic abundance without introducing some nonthermal production mechanism.

TABLE V. The scalar EWIMPs that are compatible with the result in Fig. 7. The observed DM energy density is explained by the thermal relic of the EWIMP with m_{DM} shown in the fourth column.

(n, Y)	C_1	C_2	m_{DM} [TeV]
$(3, 0)_{\text{real}}$	0	0.25	2.5 [34]
(3,0)	0	0.5	1.55 [35]
(3,1)	0.75	0.5	1.6 [34]
$(4, \frac{1}{2})$	0.25	1.25	2.4 [34]
$(4, \frac{3}{2})$	2.25	1.25	2.9 [34]
$(5, 0)_{\text{real}}$	0	1.25	9.4 [34]

IV. CONCLUSION

In this paper, we have discussed the indirect search for EWIMPs at future 100 TeV hadron colliders based on the precision measurement of the production processes of a charged lepton pair and that of a charged lepton and a neutrino. In particular, we have demonstrated that we can not only discover the EWIMPs, but also determine their properties such as their masses, $SU(2)_L$ and $U(1)_Y$ charges, and spins via the processes of our concern. This is based on two facts: the high-energy lepton production channel enables us to study its momentum distribution in great detail, and the EWIMP correction shows characteristic features, including a dip-like structure in the final-state invariant mass distribution. The latter feature also helps us to distinguish the EWIMP signals from backgrounds and systematic errors, as they are not expected to show a dip-like structure. In order to fully exploit the differences between the distributions of the EWIMP signals and systematic errors, we have adopted a fitting-based analysis as our statistical treatment.

First, we have shown in Fig. 3 the detection reach of the Higgsino and wino from the NC processes (mediated by a photon or Z boson), CC processes (mediated by a W boson), and the combination of these two results. We have seen that the addition of the CC processes improves the detection reach from the previous analysis [14]. From the combined analysis, the bounds at the 5σ (95% C.L.) level for the Higgsino and wino are 850 GeV (1.7 TeV) and 1.3 TeV (2.3 TeV), respectively. This result, in particular that for a short-lifetime Higgsino, indicates the importance of our method for the EWIMP search.

Next, we have considered the determination of the mass and $SU(2)_L$ and $U(1)_Y$ charges of the observed EWIMP. By combining the NC and CC events, the position and height of the dip in the EWIMP effect on the cross section gives us enough information to determine all three parameters. In Figs. 5 and 6, we have shown plots of the test statistics that test the validity of several choices of

parameters. As a result, the $SU(2)_L$ charge of the observed signal is correctly identified under the assumption of a single EWIMP multiplet, and the $U(1)_Y$ charge and mass are also determined precisely. In order to determine the EWIMP spin, we have plotted the contours of the test statistics that test the validity of the scalar EWIMP models with some fixed values of masses and charges. The results are shown in Figs. 7 and 8, which reveal that the spin is not completely determined by using our method alone. Using another approach to determine the EWIMP properties, or some assumption like that the observed signal corresponds to the dark matter in our Universe, may help us to obtain further information regarding the EWIMP spin.

ACKNOWLEDGMENTS

This work was supported by JSPS KAKENHI Grant Nos. 16K17715 (T. A.), 17J00813 (S. C.), 16H06490 (T. M.), and 18K03608 (T. M.).

[1] M. Cirelli, A. Strumia, and M. Tamburini, Cosmology and astrophysics of minimal dark matter, Nucl. Phys. **B787**, 152 (2007).
[2] N. Arkani-Hamed, A. Delgado, and G. F. Giudice, The well-tempered neutralino, Nucl. Phys. **B741**, 108 (2006).
[3] J. Hisano, S. Matsumoto, M. Nagai, O. Saito, and M. Senami, Non-perturbative effect on thermal relic abundance of dark matter, Phys. Lett. B **646**, 34 (2007).
[4] T. Moroi, M. Nagai, and M. Takimoto, Non-thermal production of Wino dark matter via the decay of long-lived particles, J. High Energy Phys. 07 (2013) 066.
[5] M. Beneke, A. Bharucha, F. Dighera, C. Hellmann, A. Hryczuk, S. Recksiegel, and P. Ruiz-Femenia, Relic density of wino-like dark matter in the MSSM, J. High Energy Phys. 03 (2016) 119.
[6] M. Cirelli, N. Fornengo, and A. Strumia, Minimal dark matter, Nucl. Phys. **B753**, 178 (2006).
[7] M. Cirelli and A. Strumia, Minimal dark matter: Model and results, New J. Phys. **11**, 105005 (2009).
[8] H. Baer, A. Mustafayev, and X. Tata, Monojets and mono-photons from light higgsino pair production at LHC14, Phys. Rev. D **89**, 055007 (2014).
[9] D. S. M. Alves, J. Galloway, J. T. Ruderman, and J. R. Walsh, Running electroweak couplings as a probe of new physics, J. High Energy Phys. 02 (2015) 007.
[10] C. Gross, O. Lebedev, and J. M. No, Drell-Yan constraints on new electroweak states: LHC as a $pp \to l^+l^-$ precision machine, Mod. Phys. Lett. A **32**, 1750094 (2017).
[11] M. Farina, G. Panico, D. Pappadopulo, J. T. Ruderman, R. Torre, and A. Wulzer, Energy helps accuracy: Electroweak precision tests at hadron colliders, Phys. Lett. B **772**, 210 (2017).
[12] K. Harigaya, K. Ichikawa, A. Kundu, S. Matsumoto, and S. Shirai, Indirect probe of electroweak-interacting particles at future lepton colliders, J. High Energy Phys. 09 (2015) 105.
[13] S. Matsumoto, S. Shirai, and M. Takeuchi, Indirect probe of electroweakly interacting particles at the high-luminosity large hadron collider, J. High Energy Phys. 06 (2018) 049.
[14] S. Chigusa, Y. Ema, and T. Moroi, Probing electroweakly interacting massive particles with Drell-Yan process at 100 TeV hadron colliders, Phys. Lett. B **789**, 106 (2019).
[15] L. Di Luzio, R. Gröber, and G. Panico, Probing new electroweak states via precision measurements at the LHC and future colliders, J. High Energy Phys. 01 (2019) 011.
[16] S. Matsumoto, S. Shirai, and M. Takeuchi, Indirect Probe of Electroweak-Interacting Particles with Mono-Lepton Signatures at Hadron Colliders, J. High Energy Phys. 03 (2019) 076.
[17] M. L. Mangano *et al.*, Physics at a 100 TeV pp Collider: Standard Model processes, CERN Yellow Rep. **3**, 1 (2017).
[18] R. Contino *et al.*, Physics at a 100 TeV pp collider: Higgs and EW symmetry breaking studies, CERN Yellow Rep. **3**, 255 (2017).
[19] T. Golling *et al.*, Physics at a 100 TeV pp collider: Beyond the Standard Model phenomena, CERN Yellow Rep. **3**, 441 (2017).
[20] M. Benedikt, M. Capeans Garrido, F. Cerutti, B. Goddard, J. Gutleber, J. M. Jimenez, M. Mangano, V. Mertens, J. A. Osborne, T. Otto, J. Poole, W. Riegler, D. Schulte, L. J. Tavian, D. Tommasini, and F. Zimmermann, Future Circular Collider, Technical Report No. CERN-ACC-2018-0058, CERN, Geneva, 2018, https://cds.cern.ch/record/2651300.
[21] CEPC-SPPC Study Group, CEPC-SPPC preliminary conceptual design report. 1. Physics and detector, CEPC-SPPC preliminary conceptual Design Report. 1. Physics and Detector.
[22] CEPC-SPPC Study Group, CEPC-SPPC preliminary conceptual design report. 2. Accelerator, CEPC-SPPC preliminary conceptual design report. 2. Accelerator.
[23] J. Alwall, M. Herquet, F. Maltoni, O. Mattelaer, and T. Stelzer, MadGraph 5: Going beyond, J. High Energy Phys. 06 (2011) 128.
[24] J. Alwall, R. Frederix, S. Frixione, V. Hirschi, F. Maltoni, O. Mattelaer, H. S. Shao, T. Stelzer, P. Torrielli, and M. Zaro, The automated computation of tree-level and next-to-leading order differential cross sections, and their matching to parton shower simulations, J. High Energy Phys. 07 (2014) 079.
[25] T. Sjöstrand, S. Ask, J. R. Christiansen, R. Corke, N. Desai, P. Ilten, S. Mrenna, S. Prestel, C. O. Rasmussen, and P. Z. Skands, An introduction to PYTHIA 8.2, Comput. Phys. Commun. **191**, 159 (2015).
[26] J. de Favereau, C. Delaere, P. Demin, A. Giammanco, V. Lemaître, A. Mertens, and M. Selvaggi, DELPHES 3, A

modular framework for fast simulation of a generic collider experiment, J. High Energy Phys. 02 (2014) 057.
[27] R. D. Ball, V. Bertone, S. Carrazza, L. Del Debbio, S. Forte, A. Guffanti, N. P. Hartland, and J. Rojo, Parton distributions with QED corrections, Nucl. Phys. **B877**, 290 (2013).
[28] M. Aaboud *et al.*, Search for a new heavy gauge boson resonance decaying into a lepton and missing transverse momentum in 36 fb^{-1} of pp collisions at $\sqrt{s} = 13$ TeV with the ATLAS experiment, Eur. Phys. J. C **78**, 401 (2018).
[29] A. M. Sirunyan *et al.*, Search for high-mass resonances in final states with a lepton and missing transverse momentum at $\sqrt{s} = 13$ TeV, J. High Energy Phys. 06 (2018) 128.
[30] T. Aaltonen *et al.*, Search for new particles decaying into dijets in proton-antiproton collisions at s∗∗(1/2) = 1.96-TeV, Phys. Rev. D **79**, 112002 (2009).
[31] G. Cowan, K. Cranmer, E. Gross, and O. Vitells, Asymptotic formulae for likelihood-based tests of new physics, Eur. Phys. J. C **71**, 1554 (2011); **73**, 2501 (2013).
[32] A. Buckley, J. Ferrando, S. Lloyd, K. Nordstrm, B. Page, M. Rfenacht, M. Schnherr, and G. Watt, LHAPDF6: Parton density access in the LHC precision era, Eur. Phys. J. C **75**, 132 (2015).
[33] M. Tanabashi *et al.*, Review of particle physics, Phys. Rev. D **98**, 030001 (2018).
[34] M. Farina, D. Pappadopulo, and A. Strumia, A modified naturalness principle and its experimental tests, J. High Energy Phys. 08 (2013) 022.
[35] E. Del Nobile, M. Nardecchia, and P. Panci, Millicharge or decay: A critical take on minimal dark matter, J. Cosmol. Astropart. Phys. 04 (2016) 048.